

Velocity-tunable exciton-photon hybridization in cathodoluminescence

Sven Ebel ¹, Martin Nørgaard ¹, Christian Nicolaisen Hansen ¹, N. Asger Mortensen ^{1,2} and Sergii Morozov ^{1,*}

¹*POLIMA—Center for Polariton-driven Light–Matter Interactions,*

University of Southern Denmark, Campusvej 55, DK-5230 Odense M, Denmark

²*Danish Institute for Advanced Study, University of Southern Denmark, Campusvej 55, DK-5230 Odense M, Denmark*

(Dated: March 17, 2026)

Abstract. Exciton–photon hybridization is typically realised in geometrically defined optical cavities, where tunability is achieved by modifying either the cavity or the excitonic medium. Here we investigate transition-radiation interferences in suspended subwavelength films resembling a free-electron-defined resonance and explore their interaction with excitons in transition metal dichalcogenides. We demonstrate that these resonances hybridize with excitonic transitions and can be tuned continuously by varying the electron energy. The resulting detuning depends on both film thickness and electron velocity, establishing the latter as an external and continuous knob for exciton–photon coupling. This approach enables tunable hybridization without structural modification and provides a free-electron-driven nanoscale platform for studying exciton–light interactions.

INTRODUCTION

Hybridization between excitons and confined optical modes provides a powerful route to engineer mixed light–matter states with tailored spectral and dynamical properties [1]. A broad range of resonant architectures has been developed to realise such interactions, including planar Fabry–Pérot microcavities [2], photonic crystals [3], plasmonic resonators [4, 5], Mie resonators [6, 7], and bound states in the continuum [8, 9]. These platforms provide field confinement and spectral selectivity across multiple length scales, enabling hybridization with diverse excitonic media. Tunability in these systems is commonly achieved by modifying the cavity geometry, ranging from controlling the thickness and lateral extent of Fabry–Pérot resonators [10–12] to tailoring the dimensions and arrangement of nanoscale resonators [13]. Alternatively, tuning can be realised by engineering the excitonic medium itself, for example through electrical gating [14–16] or chemical control [17, 18].

More generally, hybridization does not rely on a specific cavity design, but rather on the presence of a well-defined optical eigenmode. Such modes may be supported by an external resonator or arise intrinsically from the geometry and dielectric contrast of the structure, giving rise to so-called self-hybridized exciton–photon systems [19–22]. The van der Waals (vdW) semiconductors are particularly well suited in this regime, as their large exciton oscillator strengths and strong dielectric contrast support intrinsic optical modes that readily couple to excitonic resonances [23–28]. However, in self-hybridized systems the scope for active tuning remains inherently limited, since the optical mode is largely fixed by the geometry of the structure.

While optical spectroscopy has been central to es-

tablishing cavity and self-hybridized platforms, accessing hybridization at the nanoscale often requires probes that combine broadband excitation with nanometer spatial resolution. Free-electron-based spectroscopies meet these requirements and have therefore emerged as powerful tools for investigating exciton–photon hybrid systems in real space [29–34]. Cathodoluminescence (CL) microscopy provides high spatial and spectral resolution and has been used to map plasmon–exciton hybridization [35] as well as the impact of geometric confinement on exciton–light hybridization [36].

Here we investigate transition radiation (TR), the emission generated when an energetic free electron crosses an interface between two media [37, 38], in the presence of excitons in transition metal dichalcogenide (TMD) thin films. In thin films, TR emitted at the two interfaces can interfere constructively, giving rise to free-electron-defined resonances [39–42], whose spectral position is tunable via the electron velocity. We show that TR resonances in subwavelength dispersive films hybridize with the excitonic response at electron energies typical of scanning electron microscopy. The resulting spectral response depends on the incident electron energy, enabling velocity–tunable exciton–photon hybridization without any geometric modification of the cavity. This free-electron-tunable platform therefore provides a route to tunable exciton–photon hybridization.

RESULTS

Transition radiation resonances

We consider a free electron with velocity v_{el} normally traversing a thin film of thickness d and wavelength-dependent complex-valued isotropic dielectric function $\epsilon(\lambda)$, freely suspended in vacuum [Fig. 1(a)]. An electron interacting with such a system generates TR at each film

* Corresponding author: semo@mci.sdu.dk

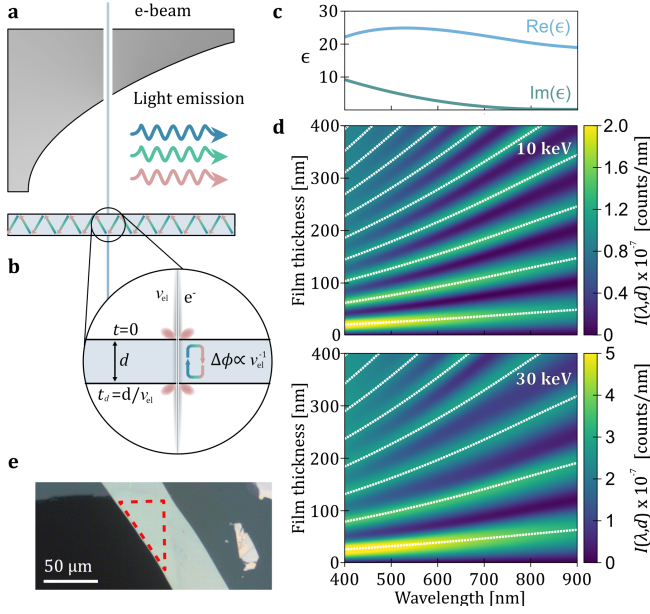


FIG. 1: Transition radiation resonances. (a) Experimental setup showing a parabolic mirror positioned in the electron beam path to collect the generated transition radiation (TR) and direct it to a spectrometer. (b) Schematic illustration of electron-velocity-dependent resonant TR in thin films of thickness d . (c) Dielectric function of a model semiconductor with a bandgap of 1.5 eV. (d) Calculated TR intensity for dielectric films described by the dielectric response shown in panel (c), plotted as a function of film thickness d and emission wavelength for electron energies of 10 and 30 keV. (e) Optical image of a suspended 83 nm thick WS_2 crystal. The red dashed line marks the suspended region.

interface as well as Cherenkov radiation within the film. An analytical treatment of this problem was developed by Ritchie and Eldridge [38]. For normal electron-beam incidence, the intensity per incident electron, emitted into a unit solid angle at polar angle θ and per unit wavelength λ in the backward direction relative to the electron trajectory, is given by:

$$I(\theta, \lambda, d, \beta) = \frac{\alpha\beta^2}{\pi^2\lambda} \mu^2(1 - \mu^2) \left| \frac{\gamma}{\Delta} \right|^2 \quad (1)$$

with

$$\begin{aligned} \gamma = & \left[\frac{\epsilon - \beta\sigma}{1 - \mu^2\beta^2} - \frac{1}{1 + \beta\sigma} \right] (\mu\epsilon + \sigma) e^{-it\sigma} \\ & + \left[-\frac{\epsilon + \beta\sigma}{1 - \mu^2\beta^2} + \frac{1}{1 - \beta\sigma} \right] (\mu\epsilon - \sigma) e^{it\sigma} \quad (2) \\ & - 2\sigma \left[\frac{\epsilon}{1 + \beta\mu} - \frac{1 - \beta\epsilon\mu}{1 - \beta^2\sigma^2} \right] e^{it/\beta}, \end{aligned}$$

and $\sigma = (\epsilon - 1 + \mu^2)^{\frac{1}{2}}$, $\beta = v_{\text{el}}/c$, $\mu = \cos\theta$, $t = 2\pi d/\lambda$, $\Delta = (\mu\epsilon - \sigma)^2 e^{it\sigma} - (\mu\epsilon + \sigma)^2 e^{-it\sigma}$, c the speed of light, and α the fine structure constant. Eq. (2) shows that the total emitted radiation comprises contributions from

Cherenkov radiation and TR formed at the two film interfaces. Yamamoto *et al.* [40] performed a similar analysis and demonstrated that, in the limit where the Cherenkov radiation contribution is negligible, the observed intensity reduces to the superposition of the TR emitted at the upper and lower interfaces (see Supplementary Note S1). Constructive interference between those terms occurs when the phase condition $\phi = t\sigma + \frac{t}{\beta} = 2\pi(m - \frac{1}{2})$ is satisfied, where m is an integer. This condition is illustrated in Fig. 1(b) and shows that the phase delay $\Delta\phi$ between successive TR excitation events is governed by the film thickness and the electron velocity. From this phase condition, we derive an expression for the resonance energy:

$$E_{\text{ph}} = \frac{h v_{\text{el}}}{d} \left(m - \frac{1}{2} \right) \left(1 + \frac{v_{\text{el}}}{c} \sqrt{\epsilon - \sin^2\theta} \right)^{-1}. \quad (3)$$

We next evaluate Eq. (1) for a dispersive dielectric film described by a model dielectric function representative of a generic semiconductor [see Eq. (4) in Methods and Fig. 1(c)], as a function of film thickness and electron energy. The results, shown in Fig. 1(d), reveal that the TR spectrum exhibits thickness-dependent resonances reminiscent of Fabry-Pérot cavity modes, characterized by standing-wave interference that produces spectral maxima and minima. In contrast to a conventional Fabry-Pérot cavity, the number of resonances exhibits a pronounced dependence on the electron velocity, with more resonances appearing over the same film-thickness range for lower electron velocities. This behaviour of the TR resonance is well captured by Eq. (3), which accurately reproduces both the thickness and electron-energy dependence of the constructive interference resonances, as indicated by the white overlays in Fig. 1(d).

Probing transition radiation resonances

To experimentally validate the TR model and examine its interaction with excitonic transitions, we use vdW materials. This material class offers both dispersive systems without additional sharp excitonic features and semiconducting compounds with pronounced excitonic resonances, while enabling straightforward fabrication and thickness control in suspended thin films. The experimental setup, schematically shown in Fig. 1(a), is based on a scanning-electron microscope (SEM) operating in a configuration with a Schottky field-emission beam and equipped with a parabolic mirror positioned above the sample stage. The mirror features a central aperture for free passage of the electron beam and collects the generated CL, which is subsequently directed to the optical detection system. As illustrated in Fig. 1(e), selected vdW crystals were transferred onto transmission electron microscopy (TEM) windows such that the crystals are freely suspended, providing two parallel vacuum-vdW material

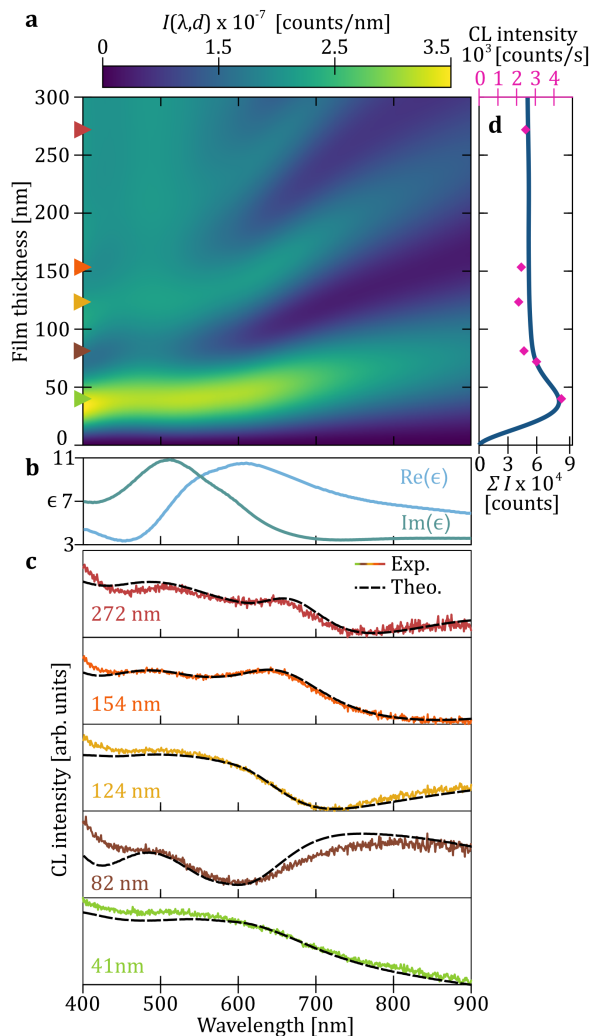


FIG. 2: Transition radiation from NbSe₂ films.

(a) Calculated TR intensity from NbSe₂ films as a function of film thickness d and emission wavelength for a free-electron energy of 30 keV. (b) Experimental in-plane dielectric function of NbSe₂ as reported by Munkhbat *et al.* [43]. (c) Experimental CL spectra at 30 keV and corresponding theoretical TR spectra for NbSe₂ films with thicknesses of 272, 154, 124, 82, and 41 nm. The selected thicknesses are indicated by triangles in panel (a). (d) Spectrally integrated experimental CL (pink diamonds) and theoretical TR (blue) intensities. In the experiments, the beam current was kept at 1.4 nA and the exposure time was 90 s.

interfaces during the measurements. The thickness of the selected crystals was determined by optical reflectivity measurements, allowing us to determine the thickness with an error margin of ± 2 nm (see Methods and Supplementary Note S2 for more details). This deterministic fabrication procedure enables efficient selection of crystals with the desired thickness and lateral size.

We first investigate niobium diselenide (NbSe₂) as a dispersive reference system to test the TR model of Eq. (1). NbSe₂ is a semimetal characterized by a

strongly dispersive dielectric function, exhibiting low optical losses towards the infrared spectral region and increased losses in the blue spectral region, the latter attributed to absorption channels arising from intraband transitions [43, 44]. Previous CL studies have shown that the bulk CL response of NbSe₂ is dominated by TR, allowing contributions from other CL generation mechanisms to be neglected in the present analysis [45]. Figure 2(a) shows the TR intensity calculated from Eq. (1) for NbSe₂ films as a function of film thickness at an electron energy of 30 keV. The in-plane dielectric function of NbSe₂ used in the calculations [Fig. 2(b)] was obtained from spectroscopic ellipsometry measurements reported by Munkhbat *et al.* [43]. The calculations in Fig. 2(a) reveal that the TR spectrum exhibits the expected resonant behaviour in the low-loss spectral region, forming distinct thickness-dependent interference maxima and minima. In contrast, the high-loss spectral region is characterized by a reduced interference contrast, indicating the suppression of interference due to increased optical losses.

We experimentally probe this behaviour by measuring a series of suspended NbSe₂ crystals with different thicknesses (indicated by coloured triangles in Fig. 2(a)). Fig. 2(c) compares the calculated and measured CL spectra for crystals with thicknesses of 274, 154, 124, 82, and 41 nm. Each measured CL spectrum is plotted alongside the corresponding calculated TR spectrum, demonstrating good agreement and capturing the characteristic interference features of the TR response. All experimental TR spectra are normalized and aligned to the theoretical TR spectrum at 600 nm, corresponding to the spectral region of highest sensitivity of our detection system. Consequently, the largest deviations between experimental and theoretical spectra are observed towards the blue spectral region, which coincides with the lowest detection sensitivity and with the general increase of the TR intensity scaling as $1/\lambda$. Another source of deviation arises from the finite out-of-plane dielectric response of vdW materials [46], which is not captured by the isotropic model considered here.

Finally, Fig. 2(d) shows the spectrally integrated TR intensity as a function of film thickness, overlaid with the corresponding spectrally integrated CL intensity, again demonstrating good agreement between the theoretical TR response and the experimental measurements. Notably, the intensity exhibits an approximately twofold enhancement for few-nanometer-thick films, corresponding to the first-order interference maximum. This behaviour arises from the lossy nature of NbSe₂, which leads to damping of higher-order resonances, while the first-order resonance remains weakly dispersive at small thicknesses.

Hybridization with excitons

Having established that Eq. (1) accurately describes the CL response of subwavelength dispersive films, we now examine how excitons modify the TR response. As a model system, we investigate molybdenum disulfide (MoS_2), a semiconducting vdW material whose bulk CL response exhibits pronounced excitonic transitions [45]. MoS_2 features A and B excitons at 672 nm and 612 nm, respectively, as extracted from the in-plane dielectric function measured by spectroscopic ellipsometry by Ermolaev *et al.* [47] and shown in Fig. 3(b). Fig. 3(a) shows the calculated TR spectrum of MoS_2 films as a function of film thickness. As in the case of NbSe_2 , thickness-dependent resonant features characteristic of the TR response of a dispersive film are observed. In contrast to NbSe_2 , however, the TR spectrum of MoS_2 exhibits pronounced spectral dips within the resonance structure that coincide with the excitonic resonances.

Experimentally, we probe this behaviour by measuring the CL response of suspended MoS_2 crystals with thicknesses selected to sample on- and off-resonant TR conditions. Fig. 3(c) shows the CL spectra of MoS_2 crystals with thicknesses of 6, 32, 85, 113, and 131 nm. The 32 nm and 113 nm crystals correspond to the expected maxima of the first- and second-order TR resonances, respectively. For all thicknesses, the measured CL spectra agree well with the analytically calculated TR response, reproducing both the thickness-dependent resonances and the modifications induced by the A and B excitons. Similar exciton-related dips with adjacent maxima have previously been reported in CL studies of thin WSe_2 crystals by Taleb *et al.* [36], where they were attributed to hybridization between excitonic resonances and the waveguide modes of the crystal.

A closer analysis of the CL spectra in Fig. 3(c) reveals that the spectral positions of the features surrounding the exciton energy depend on the crystal thickness. For the resonant crystals (32 and 113 nm), the spectral dips coincide with the exciton energy, whereas the off-resonant crystals (6, 85, and 131 nm) exhibit spectrally shifted dips. This behaviour indicates that matching or detuning the TR resonance relative to the exciton energy modifies the excitonic contribution to the CL spectrum, consistent with hybridization between the TR resonance and the exciton.

Analogous to the analysis for NbSe_2 , Fig. 3(d) shows the spectrally integrated TR intensity as a function of film thickness, overlaid with the corresponding CL intensity. The measured spectrally integrated CL intensities agree well with theory and confirm that the first-order resonance enhances the CL response for MoS_2 crystals with thicknesses around 32 nm.

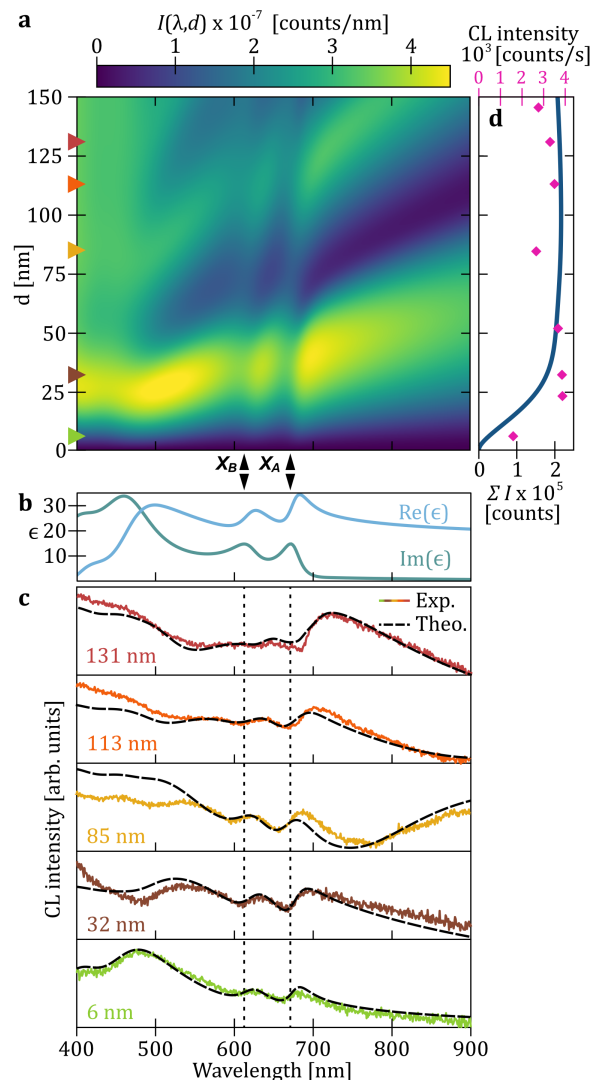


FIG. 3: Transition radiation from MoS_2 films. (a) Calculated TR intensity from MoS_2 films as a function of film thickness d and emission wavelength for a free-electron energy of 30 keV. (b) Experimental in-plane dielectric function of MoS_2 as reported by Ermolaev *et al.* [47]. (c) Experimental CL spectra at 30 keV and corresponding theoretical TR spectra for MoS_2 films with thicknesses of 131, 113, 85, 32, and 6 nm. The selected thicknesses are indicated by triangles in (a). (d) Spectrally integrated experimental CL (pink diamonds) and theoretical TR (blue) intensities. In the experiments, the beam current was kept at 1.4 nA and the exposure time was 90 s.

Electron-energy-controlled detuning

To further investigate the tunability of hybridization between TR resonances and excitons, we turn to thin tungsten disulfide (WS_2) crystals. Compared to MoS_2 , WS_2 exhibits stronger excitonic oscillator strengths and more spectrally isolated A and B excitons, enabling a clearer spectral separation of the hybridized features.

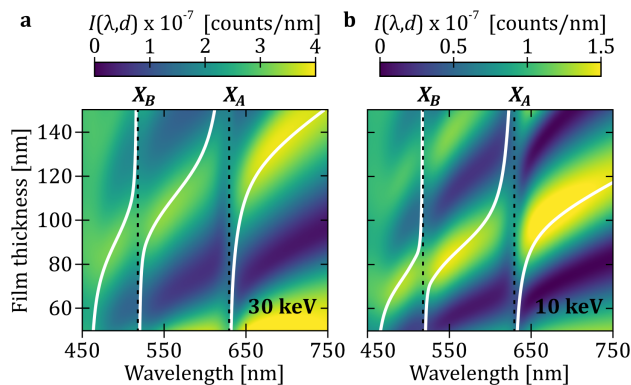


FIG. 4: Electron-energy dependent hybridization of TR resonances and excitons in WS_2 films. Calculated TR intensity spectra from WS_2 films as a function of film thickness d and emission wavelength for free-electron energies of (a) 30 keV and (b) 10 keV. Black dashed lines indicate the spectral positions of the A and B excitons in WS_2 . White solid lines show coupled-oscillator fits to the calculated TR resonance maxima.

WS_2 features A and B excitons at 630 nm and 518 nm, respectively, as extracted from the in-plane dielectric function measured by Munkhbat *et al.* [24]. Fig. 4 shows the calculated TR spectrum of WS_2 films as a function of thickness for electron energies of 10 and 30 keV, with the exciton positions indicated by black dashed lines. Here we investigate WS_2 films in the thickness range of 50–150 nm, which corresponds to the regime of the second-order TR resonance ($m = 2$). For both electron energies, the TR resonance exhibits a pronounced bending of the resonance maximum near the exciton energies, consistent with the formation of hybridized light–matter states. This behaviour is reproduced by coupled-oscillator calculations (see Methods), in which the resonance energy obtained from Eq. (3) is coupled to the excitonic transitions of WS_2 .

Changing the electron energy shifts the TR resonance according to Eq. (3), thereby modifying its dispersion. Consequently, the bending of the resonance maximum occurs at different film thicknesses, reflecting the tunability of the TR resonance relative to the exciton energies. Within the coupled-oscillator framework, this behaviour appears as a shift of the hybridized features with changing electron energy. Together, these results establish electron energy as a continuous and controllable parameter for tuning the TR resonance across the excitonic transitions.

We first probe electron-energy control of the hybridized response in an 83 nm thick WS_2 crystal. The calculated TR spectrum [Fig. 5(a)] shows that varying the electron energy tunes the TR resonance through the A-exciton energy. Consistent with this prediction, CL spectra acquired between 10 and 30 keV (in 1 keV steps) repro-

duce the same dispersion trend [Fig. 5(b)]. Representative spectra in Fig. 5(d) illustrate the evolution from a detuned, Lorentzian-like excitonic peak at 30 keV to an asymmetric line shape at intermediate energies (20 and 15 keV), and finally to a pronounced dip accompanied by two adjacent maxima when the TR resonance overlaps spectrally with the A exciton at 10 keV. The largest deviation from the calculated TR response occurs at 10 keV between 650 and 750 nm, where the measured intensity exceeds the prediction, likely due to additional incoherent contributions that become more prominent at low electron energies (Supplementary Note S3). A distinct behaviour is observed near the B exciton, where the spectra exhibit a dip fixed at the exciton energy with two adjacent maxima that shift to lower energies as the acceleration voltage decreases. Concurrently, the higher-energy maximum decreases in amplitude while the lower-energy maximum increases, consistent with tuning the TR resonance through the B-exciton energy. To quantify this behaviour, we extract the energies of the maxima from the full data set [Fig. 5(c)]. A coupled-oscillator model reproduces the measured dispersion using coupling strengths of 250 meV (TR resonance–A exciton) and 200 meV (TR resonance–B exciton), confirming that the evolving maxima originate from hybridized states formed by the interaction of the TR resonance with the excitonic transitions in WS_2 .

For a thicker 100 nm WS_2 crystal, the TR resonance can be tuned across the A-exciton energy within the accessible electron-energy range [Fig. 5(e)]. The corresponding CL spectra acquired between 10 and 30 keV (in 1 keV steps) reproduce the tuning trend [Fig. 5(f)], and representative spectra are shown in Fig. 5(h). In contrast to the 83 nm crystal, the A-exciton region is already characterised by a dip-like feature at high electron energies, accompanied by two adjacent maxima. As the electron energy is reduced, the dip shifts toward the A-exciton energy and becomes centred at 10 keV, while both maxima redshift, with the lower-energy maximum exhibiting the stronger shift. To quantify this evolution, we again extract the energies of the maxima and compare them to the coupled-oscillator model. The extracted dispersion shows good agreement with the model and reveals an increasingly asymmetric redshift below ~ 20 keV, consistent with tuning through the excitonic resonance. Around the B exciton, the response corresponds to the inverse detuning scenario compared with the A-exciton behaviour in the 83 nm crystal, and a predominantly Lorentzian-like peak is recovered at the B-exciton energy at intermediate electron energies [Fig. 5(h)].

The electron-energy tunability of TR resonances depends on the resonance order m . While the 83 nm and 100 nm crystals probe the second-order resonance ($m = 2$), thinner films enter the first-order regime ($m = 1$), for which Eq. (3) predicts a reduced energy tunability due to the $(m - 1/2)$ dependence. Consequently, the $m = 1$

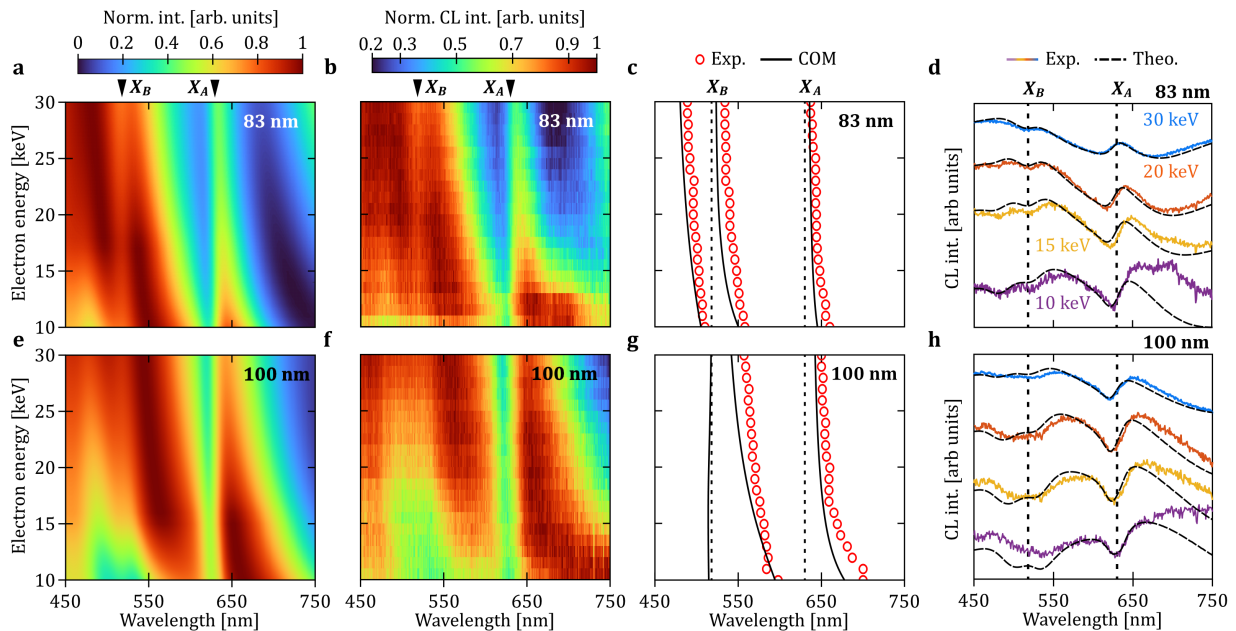


FIG. 5: Tunable hybridization between TR resonances and excitons in WS_2 films. (a,e) Calculated electron-energy-dependent TR spectra for WS_2 films with thicknesses of 83 nm (a) and 100 nm (e). (b,f) Measured electron-energy-dependent CL spectra for WS_2 films with thicknesses of 83 nm (b) and 100 nm (f). (c,g) Extracted experimental spectral positions of the intensity maxima in the CL spectra (red circles). Black solid lines show solutions of the coupled-oscillator model (COM) illustrating the tunability of the TR–exciton hybridization with electron energy. (d,h) Experimental CL spectra from WS_2 films with thicknesses of 83 nm (d) and 100 nm (h) acquired at electron energies of 30, 20, 15, and 10 keV. The spectra are normalized around 600 nm and compared to calculated TR spectra of the same thickness and electron energy. During the measurements, the beam current was maintained at 1.4 nA, with exposure times of 90–120 s.

resonance exhibits a comparatively flat dispersion and, in turn, only weak tuning of the hybridized spectral features can be expected. This behaviour is confirmed by additional measurements on a 55 nm thick flake, presented in Supplementary Note S4.

DISCUSSION

In this work, we have demonstrated that TR resonances supported by suspended subwavelength dispersive films provide a versatile platform for exciton–photon hybridization under free-electron excitation. We show that the spectral response of TR can be tuned continuously through excitonic transitions by varying either the film thickness or the electron energy. This enables controlled detuning between the photonic resonance and excitons in TMD thin films, resulting in spectral features consistent with hybridized light–matter states.

In contrast to conventional cavity platforms, where tunability is typically achieved through geometric modification of the resonator or active control of the excitonic medium, the present approach introduces the electron energy as an external and continuous tuning parameter. The TR interference thus acts as an electron-defined optical resonance whose dispersion can be engineered without

altering the physical structure of the film. This capability is particularly relevant for self-hybridized systems in vdW semiconductors, where the intrinsic optical mode is otherwise fixed by geometry.

More broadly, these results establish TR resonances under electron-beam excitation as a platform for studying tunable hybrid light–matter interactions. The ability to manipulate the photonic resonance via electron velocity, while simultaneously leveraging nanometer spatial resolution, opens new opportunities for probing exciton–photon coupling in engineered self-hybridized photonic systems [48, 49]. Beyond these systems, this approach may be extended to cavities formed by vdW heterostructures, where electron-controlled tuning of optical eigenmodes could provide additional flexibility for investigating exciton–light interactions in complex layered architectures [50].

METHODS

CL measurements

CL measurements were performed in a TESCAN MIRA3 instrument equipped with a Schottky field-emission gun and a SPARC Spectral detection system

(Delmic). Acceleration voltages between 5 and 30 kV were used with a beam current of 1.4 nA, measured using a Faraday cup. The CL signal was collected by an aluminium-coated parabolic mirror with a central aperture for the electron beam. The mirror provides an effective numerical aperture of 0.97 for collecting generated CL signals. The collected CL was directed to a spectrograph (Andor Kymera 193i) equipped with a 150 lines/mm (500 nm blaze) grating and detected using a CCD camera (Andor Newton). Spectra were acquired with exposure times of 90–120 s using a beam spot size of approximately 10 nm to ensure adequate signal-to-noise ratio. Angle-resolved maps were recorded with 90 s exposure times. All CL spectra and angular maps were background-corrected using dark counts acquired with the electron beam blanked and afterward corrected for the system response function of the instrument [45].

Sample fabrication

The investigated vdW materials were purchased from HQ Graphene. Samples were prepared by mechanical exfoliation and transferred onto polydimethylsiloxane (PDMS) stamps, enabling deterministic placement using a viscoelastic stamping technique [51]. We utilized TEM windows in a silicon nitride (Si_3N_4) covered silicon (Si) wafers as target substrates, allowing the selected vdW crystals to be freely suspended while supported at the window edges. Si_3N_4 film over the windows was removed to enable the free suspension of vdW crystals. For deterministic transfer, the substrate was heated to 110°C during contact to promote release of the flake from the PDMS stamp. The thickness of the fabricated suspended vdW crystals was measured with optical reflection spectroscopy (For details see Supplementary Note S2).

Dielectric function of a model semiconductor

We treat the causal optical response of a model semiconductor by calculating the complex dielectric function [52]

$$\epsilon(\omega) = \frac{2D}{\pi} \left[-\frac{(E_g)^2}{(\hbar\omega + i\Gamma)^2} \ln\left(\frac{E_c}{E_g}\right) + \frac{1}{2} \left(1 + \frac{E_g}{\hbar\omega + i\Gamma}\right)^2 \ln\left(\frac{\hbar\omega + i\Gamma + E_c}{\hbar\omega + i\Gamma + E_g}\right) + \frac{1}{2} \left(1 - \frac{E_g}{\hbar\omega + i\Gamma}\right)^2 \ln\left(\frac{\hbar\omega + i\Gamma - E_c}{\hbar\omega + i\Gamma - E_g}\right) \right], \quad (4)$$

where E_g is the bandgap energy and E_c the cut-off energy. Furthermore, Γ corresponds to the lifetime broadening and D represents an overall strength that is independent of the photon energy. Calculations in Fig. 1

are based on $E_g = 1.5$ eV, $E_c = 6$ eV, $\Gamma = 40$ meV, and $D = 60$.

Coupled-oscillator model

To discuss our analytical and theoretical results in the context of photon-exciton hybridization we apply a minimal coupled-oscillator model (see e.g. [53, 54]),

$$\begin{bmatrix} E_{\text{ph}} & \hbar\Omega_A/2 & \hbar\Omega_B/2 \\ \hbar\Omega_A/2 & E_A & 0 \\ \hbar\Omega_B/2 & 0 & E_B \end{bmatrix} \begin{bmatrix} \alpha \\ \beta \\ \gamma \end{bmatrix} = \hbar\omega \begin{bmatrix} \alpha \\ \beta \\ \gamma \end{bmatrix}, \quad (5)$$

for the resonance energies $\hbar\omega$ of the model. The eigenvectors describe the relative weighting of the excitonic and photonic components. Furthermore, E_j and $\hbar\Omega_j$ denote the exciton energies and the associated coupling strength of the $j = \{A, B\}$ excitons of WS_2 . For a dispersive material $\epsilon(\omega)$, we obtain a frequency-dependent photon energy $E_{\text{ph}} = E_{\text{ph}}(\omega)$ through Eq. (3). Solving the eigenvalue problem for a dispersive material consequently leads to a nonlinear equation

$$E_{\text{ph}}(\omega) - \hbar\omega - \frac{1}{4} \sum_j \frac{(\hbar\Omega_j)^2}{E_j - \hbar\omega} = 0. \quad (6)$$

For the generally complex resonant energies obtained as solutions to this equation, we require a model of the permittivity of WS_2 that is analytically continued to complex-valued energies. Such a model is obtained by a least-squares fitting of the experimental permittivity of WS_2 reported by Munkhbat *et al.* [43], using in practice a sum of six Lorentzian oscillators (see Supplementary Note S5). The solutions ω to this nonlinear equation give the white solid lines in Fig. 4. For simplicity, the analysis assumed a fixed polar angle of $\theta = 60^\circ$.

Competing interests: The authors declare no competing financial or non-financial interests.

Funding Declaration: The Center for Polariton-driven Light-Matter Interactions (POLIMA) is sponsored by the Danish National Research Foundation (Project No. DNRF165).

Author contributions: The idea of the project was conceived by S. E and S. M. Sample preparation and CL spectroscopy measurements were handled by S. E and M. N. The coupled-oscillator model was solved by C. N. H. and S. E. The project was supervised by S. M. and N. A. M. All authors contributed to analysing the data and writing the manuscript. All authors have accepted responsibility for the entire content of this manuscript and approved its submission.

Acknowledgments: We thank P. A. D. Gonçalves and C. Tserkezis for stimulating discussions.

-
- [1] C. Schneider, M. M. Glazov, T. Korn, S. Höfling, and B. Urbaszek. Two-dimensional semiconductors in the regime of strong light-matter coupling. *Nature Communications*, 9:2695, 2018.
- [2] C. Weisbuch, M. Nishioka, A. Ishikawa, and Y. Arakawa. Observation of the coupled exciton-photon mode splitting in a semiconductor quantum microcavity. *Physical Review Letters*, 69(23):3314–3317, 1992.
- [3] L. Zhang, R. Gogna, W. Burg, E. Tutuc, and H. Deng. Photonic-crystal exciton-polaritons in monolayer semiconductors. *Nature Communications*, 9:713, 2018.
- [4] Y. Sugawara, T. A. Kelf, J. J. Baumberg, M. E. Abdelsalam, and P. N. Bartlett. Strong coupling between localized plasmons and organic excitons in metal nanovoids. *Physical Review Letters*, 97(26):266808, 2006.
- [5] W. Liu, B. Lee, C. H. Naylor, H.-S. Ee, J. Park, A. T. C. Johnson, and R. Agarwal. Strong exciton-plasmon coupling in MoS₂ coupled with plasmonic lattice. *Nano Letters*, 16(2):1262–1269, 2016.
- [6] F. Todisco, R. Malureanu, C. Wolff, P. A. D. Gonçalves, A. S. Roberts, N. A. Mortensen, and C. Tserkezis. Magnetic and electric Mie-exciton polaritons in silicon nanodisks. *Nanophotonics*, 9(4):803–814, 2020.
- [7] S. Wang, T. V. Raziman, S. Murai, G. W. Castellanos, P. Bai, A. M. Berghuis, R. H. Godiksen, A. G. Curto, and J. Gómez Rivas. Collective Mie exciton-polaritons in an atomically thin semiconductor. *Journal of Physical Chemistry C*, 124(35):19196–19203, 2020.
- [8] E. Maggolini, L. Polimeno, F. Todisco, A. Di Renzo, B. Han, M. De Giorgi, V. Ardizzone, C. Schneider, R. Mastria, A. Cannavale, M. Pugliese, L. De Marco, A. Rizzo, V. Maiorano, G. Gigli, D. Gerace, D. Sanvitto, and D. Ballarini. Strongly enhanced light-matter coupling of monolayer WS₂ from a bound state in the continuum. *Nature Materials*, 22(8):964–969, 2023.
- [9] T. Weber, L. Kühner, L. Sortino, A. Ben Mhenni, N. P. Wilson, J. Kühne, J. J. Finley, S. A. Maier, and A. Tittl. Intrinsic strong light-matter coupling with self-hybridized bound states in the continuum in van der Waals metasurfaces. *Nature Materials*, 22(8):970–976, 2023.
- [10] S. Dufferwiel, S. Schwarz, F. Withers, A. A. P. Trichet, F. Li, M. Sich, O. Del Pozo-Zamudio, C. Clark, A. Nalitov, D. D. Solnyshkov, G. Malpuech, K. S. Novoselov, J. M. Smith, M. S. Skolnick, D. N. Krizhanovskii, and A. I. Tartakovskii. Exciton-polaritons in van der Waals heterostructures embedded in tunable microcavities. *Nature Communications*, 6:8579, 2015.
- [11] D. Urbonas, T. Stöferle, F. Scafirimuto, U. Scherf, and R. F. Mahrt. Zero-dimensional organic exciton-polaritons in tunable coupled Gaussian defect microcavities at room temperature. *ACS Photonics*, 3(9):1542–1545, 2016.
- [12] L. Lackner, M. Dusel, O. A. Egorov, B. Han, H. Knopf, F. Eilenberger, S. Schröder, K. Watanabe, T. Taniguchi, S. Tongay, C. Anton-Solanas, S. Höfling, and C. Schneider. Tunable exciton-polaritons emerging from WS₂ monolayer excitons in a photonic lattice at room temperature. *Nature Communications*, 12:4933, 2021.
- [13] N. Vu Cam, M. A. Rahman, S. Akhil, E. G. Durmusoglu, T. T. H. Do, P. L. Hernandez-Martinez, C. Dabard, D. Arora, S. Uddin, G. Zamiri, H. Wang, S. T. Ha, N. A. Mortensen, H. V. Demir, and J. K. W. Yang. Tunable multi-resonant microcavity exciton-polaritons in colloidal quantum wells. *Nano Letters*, 25(15):6109–6116, 2025.
- [14] M. Sidler, P. Back, O. Cotlet, A. Srivastava, T. Fink, M. Kroner, E. Demler, and A. Imamoglu. Fermi polaron-polaritons in charge-tunable atomically thin semiconductors. *Nature Physics*, 13(3):255–261, 2016.
- [15] B. Munkhbat, D. G. Baranov, A. Bisht, M. A. Hoque, B. Karpiak, S. P. Dash, and T. Shegai. Electrical control of hybrid monolayer tungsten disulfide-plasmonic nanoantenna light-matter states at cryogenic and room temperatures. *ACS Nano*, 14(1):1196–1206, 2020.
- [16] T. Hoekstra and J. van de Groep. Electrically tunable strong coupling in a hybrid-2D excitonic metasurface for optical modulation. *Light: Science & Applications*, 15:28, 2026.
- [17] W. Ahn and B. S. Simpkins. Spectroelectrochemical measurement and modulation of exciton-polaritons. *APL Photonics*, 5(7):076107, 2020.
- [18] D. Friedrich, J. Qin, B. Schurr, T. Tufarelli, H. Groß, and B. Hecht. Anticrossing of a plasmonic nanoresonator mode and a single quantum dot at room temperature. *Advanced Science*, 12(36):e06676, 2025.
- [19] A. Canales, D. G. Baranov, T. J. Antosiewicz, and T. Shegai. Abundance of cavity-free polaritonic states in resonant materials and nanostructures. *Journal of Chemical Physics*, 154(2):024701, 2021.
- [20] L. K. van Vugt, B. Piccione, C.-H. Cho, P. Nukala, and R. Agarwal. One-dimensional polaritons with size-tunable and enhanced coupling strengths in semiconductor nanowires. *Proceedings of the National Academy of Sciences*, 108(25):10050–10055, 2011.
- [21] R. Verre, D. G. Baranov, B. Munkhbat, J. Cuadra, M. Käll, and T. Shegai. Transition metal dichalcogenide nanodisks as high-index dielectric Mie nanoresonators. *Nature Nanotechnology*, 14(7):679–683, 2019.
- [22] C. Tserkezis, P. E. Stamatopoulou, C. Wolff, and N. A. Mortensen. Self-hybridisation between interband transitions and Mie modes in dielectric nanoparticles. *Nanophotonics*, 13(14):2513–2522, 2024.
- [23] Q. Wang, L. Sun, B. Zhang, C. Chen, X. Shen, and W. Lu. Direct observation of strong light-exciton coupling in thin WS₂ flakes. *Optics Express*, 24(7):7151, 2016.
- [24] B. Munkhbat, D. G. Baranov, M. Stührenberg, M. Wersäll, A. Bisht, and T. Shegai. Self-hybridized exciton-polaritons in multilayers of transition metal dichalcogenides for efficient light absorption. *ACS Photonics*, 6(1):139–147, 2018.
- [25] F. Dirnberger, J. Quan, R. Bushati, G. M. Diederich, M. Florian, J. Klein, K. Mosina, Z. Sofer, X. Xu, A. Kamra, F. J. García-Vidal, A. Alù, and V. M. Menon. Magneto-optics in a van der Waals magnet tuned by self-hybridized polaritons. *Nature*, 620(7974):533–537, 2023.
- [26] M. Black, M. Asadi, P. Darman, S. Seçkin, F. Schillmöller, T. A. F. König, S. Darbari, and N. Talebi. Long-range self-hybridized exciton-polaritons in two-dimensional Ruddlesden-Popper perovskites. *ACS Photonics*, 11(10):4065–4075, 2024.
- [27] S. B. Anantharaman, J. Lynch, C. E. Stevens, C. Munley, C. Li, J. Hou, H. Zhang, A. Torma, T. Darlington, F. Coen, K. Li, A. Majumdar, P. J. Schuck, A. Mohite, H. Harutyunyan, J. R. Hendrickson, and D. Jariwala. Dy-

- namics of self-hybridized exciton–polaritons in 2D halide perovskites. *Light: Science & Applications*, 13:1, 2024.
- [28] J. D. Ziegler, S. Papadopoulos, A. J. Moilanen, M. Martínez, Q. Lin, K. Mosina, T. Taniguchi, K. Watanabe, Z. Sofer, F. Dimberger, and L. Novotny. Electrical excitation of self-hybridized exciton polaritons in a van der Waals antiferromagnet. *Science Advances*, 11(45):eadz6724, 2025.
- [29] M. Kociak, X. Li, Y. Auad, C. Hamon, C. Goldmann, L. Tizei, and O. Stéphan. Strong and weak coupling nanophysics with free electron beams. *Advanced Optical Materials*, 13(34):e01548, 2025.
- [30] J.-H. Song, S. Raza, J. van de Groep, J.-H. Kang, Q. Li, P. G. Kik, and M. L. Brongersma. Nanoelectromechanical modulation of a strongly-coupled plasmonic dimer. *Nature Communications*, 12:48, 2021.
- [31] A. B. Yankovich, B. Munkhbat, D. G. Baranov, J. Cuadra, E. Olsén, H. Lourenço-Martins, L. H. G. Tizei, M. Kociak, E. Olsson, and T. Shegai. Visualizing spatial variations of plasmon–exciton polaritons at the nanoscale using electron microscopy. *Nano Letters*, 19(11):8171–8181, 2019.
- [32] O. Bitton, S. N. Gupta, L. Houben, M. Kvapil, V. Krápek, T. Šíkola, and G. Haran. Vacuum Rabi splitting of a dark plasmonic cavity mode revealed by fast electrons. *Nature Communications*, 11:487, 2020.
- [33] F. Chahshouri, M. Taleb, F. K. Diekmann, K. Rossnagel, and N. Talebi. Interaction of excitons with Cherenkov radiation in WSe₂ beyond the non-recoil approximation. *Journal of Physics D: Applied Physics*, 55(14):145101, 2022.
- [34] H. C. Nerl, K. Elyas, Z. Kochovski, N. Talebi, C. T. Koch, and K. Höflich. Flat dispersion at large momentum transfer at the onset of exciton polariton formation. *Communications Physics*, 7:388, 2024.
- [35] F. Davoodi, M. Taleb, F. K. Diekmann, T. Coenen, K. Rossnagel, and N. Talebi. Tailoring the band structure of plexcitonic crystals by strong coupling. *ACS Photonics*, 9(7):2473–2482, 2022.
- [36] M. Taleb, F. Davoodi, F. K. Diekmann, K. Rossnagel, and N. Talebi. Charting the exciton–polariton landscape of WSe₂ thin flakes by cathodoluminescence spectroscopy. *Advanced Photonics Research*, 3(1):2100124, 2021.
- [37] V. L. Ginzburg. Radiation by uniformly moving sources (Vavilov–Cherenkov effect, transition radiation, and other phenomena). *Physics-Uspexhi*, 39(10):973–982, 1996.
- [38] R. H. Ritchie and H. B. Eldridge. Optical emission from irradiated foils. I. *Physical Review*, 126(6):1935–1947, 1962.
- [39] E. T. Arakawa, N. O. Davis, and R. D. Birkhoff. Temperature and thickness dependence of transition radiation from thin silver foils. *Physical Review*, 135(1A):A224–A226, 1964.
- [40] N. Yamamoto, H. Sugiyama, and A. Toda. Cherenkov and transition radiation from thin plate crystals detected in the transmission electron microscope. *Proceedings of the Royal Society A*, 452(1953):2279–2301, 1996.
- [41] X. Lin, S. Easo, Y. Shen, H. Chen, B. Zhang, J. D. Joannopoulos, M. Soljačić, and I. Kaminer. Controlling cherenkov angles with resonance transition radiation. *Nature Physics*, 14(8):816–821, 2018.
- [42] S. Fiedler, P. E. Stamatopoulou, A. Assadillayev, C. Wolff, H. Sugimoto, M. Fujii, N. A. Mortensen, S. Raza, and C. Tserkezis. Disentangling cathodoluminescence spectra in nanophotonics: Particle eigenmodes vs transition radiation. *Nano Letters*, 22(6):2320–2327, 2022.
- [43] B. Munkhbat, P. Wróbel, T. J. Antosiewicz, and T. O. Shegai. Optical constants of several multilayer transition metal dichalcogenides measured by spectroscopic ellipsometry in the 300–1700 nm range: High index, anisotropy, and hyperbolicity. *ACS Photonics*, 9(7):2398–2407, 2022.
- [44] H. M. Hill, A. F. Rigosi, S. Krylyuk, J. Tian, N. V. Nguyen, A. V. Davydov, D. B. Newell, and A. R. Hight Walker. Comprehensive optical characterization of atomically thin NbSe₂. *Physical Review B*, 98(16):165109, 2018.
- [45] S. Ebel, Y. Lebsir, T. Yezekyan, N. A. Mortensen, and S. Morozov. An atlas of photonic and plasmonic materials for cathodoluminescence microscopy. *Nanophotonics*, 14(15):2647–2671, 2025.
- [46] M. Nørgaard, T. Yezekyan, S. Rolfs, C. Frydendahl, N. A. Mortensen, and V. A. Zenin. Near-field refractometry of van der Waals crystals. *Nanophotonics*, 14(14):2473–2483, 2025.
- [47] G. A. Ermolaev, D. V. Grudin, Y. V. Stebunov, K. V. Voronin, V. G. Kravets, J. Duan, A. B. Mazitov, G. I. Tselikov, A. Bylinkin, D. I. Yakubovsky, S. M. Novikov, D. G. Baranov, A. Y. Nikitin, I. A. Kruglov, T. Shegai, P. Alonso-González, A. N. Grigorenko, A. V. Arsenin, K. S. Novoselov, and V. S. Volkov. Giant optical anisotropy in transition metal dichalcogenides for next-generation photonics. *Nature Communications*, 12:854, 2021.
- [48] L. Li, W. Li, X. Zong, and Y. Liu. Self-hybridized exciton–polaritons in perovskite-based subwavelength photonic crystals. *New Journal of Physics*, 24(8):083042, 2022.
- [49] X. Wu, S. Zhang, J. Song, X. Deng, W. Du, X. Zeng, Y. Zhang, Z. Zhang, Y. Chen, Y. Wang, C. Jiang, Y. Zhong, B. Wu, Z. Zhu, Y. Liang, Q. Zhang, Q. Xiong, and X. Liu. Exciton polariton condensation from bound states in the continuum at room temperature. *Nature Communications*, 15:3345, 2024.
- [50] S. L. Moore, H. Y. Lee, N. Rivera, Y. Karube, M. Ziffer, E. S. Yanev, T. P. Darlington, A. J. Sternbach, M. A. Holbrook, J. Pack, X. Xu, C. R. Dean, J. S. Owen, P. J. Schuck, M. Delor, X. Y. Zhu, J. Hone, and D. N. Basov. Van der Waals waveguide quantum electrodynamics probed by infrared nano-photoluminescence. *Nature Photonics*, 19(8):833–839, 2025.
- [51] A. Castellanos-Gomez, M. Buscema, R. Molenaar, V. Singh, L. Janssen, H. S. J. van der Zant, and G. A. Steele. Deterministic transfer of two-dimensional materials by all-dry viscoelastic stamping. *2D Materials*, 1(1):011002, 2014.
- [52] S. Adachi. Effects of the indirect transitions on optical dispersion relations. *Physical Review B*, 41(6):3504–3508, 1990.
- [53] P. Törmä and W. L. Barnes. Strong coupling between surface plasmon polaritons and emitters: a review. *Reports on Progress in Physics*, 78(1):013901, 2015.
- [54] C. Tserkezis, A. I. Fernández-Domínguez, P. A. D. Gonçalves, F. Todisco, J. D. Cox, K. Busch, N. Stenger, S. I. Bozhevolnyi, N. A. Mortensen, and C. Wolff. On

the applicability of quantum-optical concepts in strong-

coupling nanophotonics. *Reports on Progress in Physics*, 83(8):082401, 2020.